In situ observation of a phase transition in silicon carbide under shock compression using pulsed x-ray diffraction

S. J. Tracy,[1,*] R. F. Smith,[2] J. K. Wicks,[1,†] D. E. Fratanduono,[2] A. E. Gleason,[3] C. A. Bolme,[4] V. B. Prakapenka,[5] S. Speziale,[6] K. Appel,[7] A. Fernandez-Pañella,[2] H. J. Lee,[8] A. MacKinnon,[8,‡] F. Tavella,[8] J. H. Eggert,[2] and T. S. Duffy[1]

[1]*Department of Geosciences, Princeton University, Princeton, New Jersey 08544, USA*
[2]*Lawrence Livermore National Laboratory, Livermore, California 94550, USA*
[3]*Stanford Institute for Materials and Energy Sciences, SLAC National Accelerator Laboratory, Menlo Park, California 94025, USA*
[4]*Shock and Detonation Physics, Los Alamos National Laboratory, Los Alamos, New Mexico 87545, USA*
[5]*GeoSoilEnviroCARS University of Chicago, Argonne National Laboratory, Argonne, Illinois 60439, USA*
[6]*GFZ German Research Centre for Geosciences, Telegrafenberg, 14473 Potsdam, Germany*
[7]*European XFEL GmbH, Holzkoppel 4, D-22869 Schenefeld, Germany*
[8]*Linac Coherent Light Source, SLAC National Accelerator Laboratory, Menlo Park, California 94025, USA*

(Received 16 November 2018; revised manuscript received 5 April 2019; published 17 June 2019)

The behavior of silicon carbide (SiC) under shock compression is of interest due to its applications as a high-strength ceramic and for general understanding of shock-induced polymorphism. Here we use the Matter in Extreme Conditions beamline of the Linac Coherent Light Source to carry out a series of time-resolved pump-probe x-ray diffraction measurements on SiC laser-shocked to as high as 206 GPa. Experiments on single crystals and polycrystals of different polytypes show a transformation from a low-pressure tetrahedral phase to the high-pressure rocksalt-type (B1) structure. We directly observe coexistence of the low- and high-pressure phases in a mixed-phase region and complete transformation to the B1 phase above 200 GPa. The densities measured by x-ray diffraction are in agreement with both continuum gas-gun studies and a theoretical B1 Hugoniot derived from static-compression data. Time-resolved measurements during shock loading and release reveal a large hysteresis upon unloading, with the B1 phase retained to as low as 5 GPa. The sample eventually reverts to a mixture of polytypes of the low-pressure phase at late times. Our study demonstrates that x-ray diffraction is an effective means to characterize the time-dependent structural response of materials undergoing shock-induced phase transformations at megabar pressures.

DOI: 10.1103/PhysRevB.99.214106

I. INTRODUCTION

Silicon carbide (SiC) is an important technological material with widespread mechanical, electronic, and optical applications [1]. In particular, SiC plays a major role as a high-strength ceramic used in armoring and impact coatings [2,3]. Characterization of the dynamic response of SiC is a long-sought-after goal to improve the design and performance of impact shielding. Under ballistic impact conditions (<20 GPa), SiC provides a rigid barrier to effectively break projectiles. However, at high stress, SiC is observed to lose strength and undergo a phase transition [4,5]. SiC is also found naturally in meteorites, impact sites, diamond inclusions, and various terrestrial rock types [6,7]. As a result, there has been long-standing interest in its behavior under dynamic loading [4,5,8–11]. SiC has also been studied extensively under static high pressures and temperatures [12,13] and is often used as a model system for understanding the B3 (zincblende)–to–B1 (rocksalt) phase transition under compression [14].

Under ambient conditions, the crystal structure of SiC is a derivative of the diamond structure, with Si and C atoms linked in an sp^3 bonding network. The structure can be viewed as a framework of covalently bonded corner-linked tetrahedra. SiC exhibits a large number (>250) of polytypes based on different stacking sequences of Si-C bilayers. Major polytypes are designated 3C, 2H, 4H, and 6H. The cubic 3C polytype ($F\bar{4}3m$) adopts the B3 or zincblende structure and is known as β-SiC. The hexagonal polytypes include 2H (wurtzite) and 4H and 6H polytypes (all $P6_3mc$) and are collectively known as α-SiC. In addition, SiC readily incorporates defects and impurities [15].

Early x-ray diffraction (XRD) experiments identified a phase change under 300 K static compression to a rocksalt-type (B1) structure (space group $Fm\bar{3}m$) near 100 GPa [16]. This structural transformation involves a change from fourfold to sixfold coordination and is accompanied by large-volume collapse (∼16–20%) [16–19]. Gas-gun shock-wave experiments on 6H SiC showed evidence of a similar phase transition near 100 GPa, with a mixed-phase region extending up to ∼140 GPa [4,5]. By analogy with static experiments, the high-pressure phase was assumed to correspond to the

*Present address: Geophysical Laboratory, Carnegie Institution for Science, Washington, DC 20015, USA; sjtracy@carnegiescience.edu
†Present address: Department of Earth and Planetary Sciences, Johns Hopkins University, Baltimore, Maryland 21218, USA
‡Present address: Livermore National Laboratory, Livermore, California 94550, USA

B1 structure, but lattice-level structural information was not obtained. Density functional theory calculations predict that this phase transition occurs at lower pressures, around 60–70 GPa, and 0 K [20–22]. In addition to equilibrium structure calculations, the transformation pathway from the ambient zincblende- and wurtzite-type structures to the high-pressure rocksalt phase has been extensively investigated theoretically, with multiple proposed mechanisms and transformation pathways [14,23,24].

Recently, new attention has been focused on SiC at high pressures due to its potential presence in extrasolar carbon-rich planets [25–27]. Using a laser-heated diamond anvil cell, the B3–B1 transformation was found to occur near 60–74 GPa and ∼2000 K with a negative Clausius-Clapeyron slope [17,18]. The equation of state (EOS) of the B1 phase was also determined up to 200 GPa in static diamond anvil cell experiments [18,19]. Additionally, evidence of the decomposition of SiC at high pressure and temperature has been reported [28].

Crystallographic phase transitions occur over a finite time scale, dictated by the transformation mechanism. Due to the nanosecond time scales of laser-driven shock experiments, kinetic effects can be important. In cases where the duration of the experiment approaches this time scale, a transition may not be observed or may require significant overpressure. As a result, there has been debate regarding the conditions under which reconstructive phase transitions involving coordination changes can be inhibited on shock time scales [29–31]. In static experiments, the B3–B1 transition in SiC is observed to be reversible, exhibiting a pronounced hysteresis, with the onset of the back transformation not occurring until 35 GPa upon pressure release [16]. This hysteresis on back transformation and the overpressure required to achieve the transition in gas-gun studies indicate that both the low- and the high-pressure phases can persist outside of their equilibrium stability field for some time. Coupling laser-drive compression with the sub-nanosecond time resolution an x-ray free electron laser probe provides a new opportunity to characterize time-dependent metastability.

In this study, the structural behavior of SiC was examined using laser-driven shock compression and *in situ* XRD. Through a series of pump-probe experiments on both single crystals and polycrystals, we explore the behavior of SiC near and above the B1 phase transition. Our study provides the first direct information on the SiC structure under dynamic loading and release. Our results are compared to previous shock-wave and static compression data to provide insights into the phase stability and kinetics in this fundamental material. More generally, our work also demonstrates the utility of laser-based shock compression combined with *in situ* XRD for structural studies of materials at megabar pressures.

II. EXPERIMENTAL PROCEDURE

Laser-driven shock compression experiments were carried out at the Matter in Extreme Conditions (MEC) end station of the Linac Coherent Light Source (LCLS) [38]. Samples consisted of polycrystalline SiC in the cubic 3C form (Mitsui Corp.) and α-SiC (0001) single crystals of polytype 4H (MTI Corp). Both materials were grown by metal organic chemical vapor deposition. Samples were characterized under ambient conditions by XRD and Raman spectroscopy and the results were consistent with literature values (Supplementary Material, Figs. S1– S3 [32]).

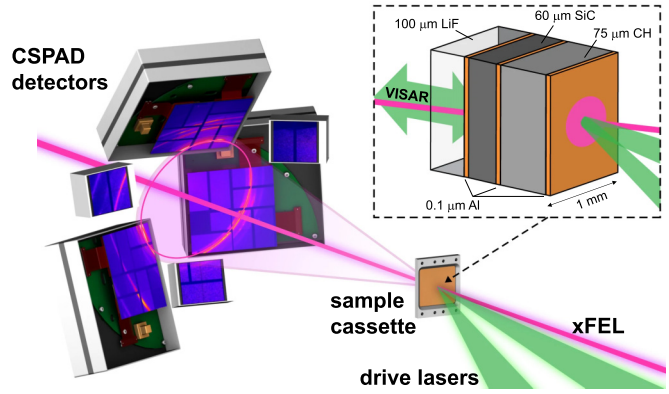

FIG. 1. Schematic of the experimental setup. Samples were mounted in a translatable cassette. The x-ray beam (xFEL) was incident at 15° relative to target normal and the two nanosecond laser arms were oriented at 6° and 25°. Diffracted x rays were recorded on CSPAD detectors. The target package, illustrated on the right, shows the CH ablator, SiC sample, and LiF window. The VISAR was oriented normal to the sample, focused on the LiF-SiC interface.

The target package design is illustrated schematically in Fig. 1. Samples were cut and polished to a thickness of 40–60 μm and glued to polyimide (CH) ablators (∼75 μm thick) with an approximately 1-μm-thick epoxy layer. A subset of samples was prepared with 100-μm-thick LiF (100) windows glued to the rear surface of the SiC. A 0.1-μm-thick Al coating was deposited on the ablation side of the CH, the CH-SiC interface, and the SiC-LiF interface. The samples were mounted on target plates with a common orientation for the single crystals.

Target packages were dynamically compressed using 30-J pulses from a 527-nm Nd:glass laser system [39] focused to a diameter of 200–250 μm (Fig. 1). The lasers were incident at 6° and 15° from target normal and overlapped on the polyimide surface to generate ablation-driven compression waves that propagated through the target package. The laser pulses were 12–15 ns long and the pulse shape (quasi-flat-top) had a modest upward ramp to maintain a steady shock in the sample as the ablation plasma expanded. Stress was controlled by tuning the laser spot size (200–250 μm). Experiments were performed both with and without phase plates. The reproducibility of the drive for a given laser energy and spot size was monitored by comparing measured pulse shapes (Supplemental Material, Fig. S4 [32]).

A line-imaging VISAR (velocity interferometer system for any reflector) was used to monitor the free surface or SiC-LiF interface velocity history of the sample [35]. The VISAR had a 300-μm field of view and a 20-ns sweep duration. For a given drive condition (laser power, focal spot size), the VISAR data from a shot using a target with a LiF window was used to determine the peak sample stress using the known equations of state of SiC and LiF (Supplemental Material, Table S1 [32]) and standard impedance matching techniques [40]. The VISAR also provided information on x-ray timing

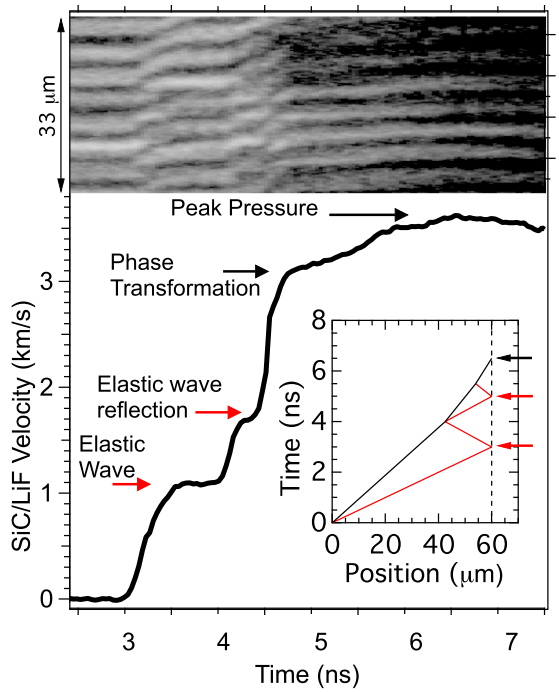

FIG. 2. Representative VISAR wave profile collected using drive conditions of the ∼114-GPa polycrystalline time series. The time axis is relative to shock entering SiC. The plateau associated with the phase transformation is at a SiC-LiF particle velocity of ∼3.1 km/s, consistent with SiC stress of ∼100 GPa. Inset: Schematic wave diagram illustrating the elastic wave (red line) arrival along with a second elastic reverberation due to an interaction between the elastic release from the LiF window and the oncoming plastic wave (black line).

and positioning as well as identifying any nonplanarity of the load. A representative VISAR trace is shown in Fig. 2. This VISAR trace was collected using the drive conditions for the 114-GPa polycrystalline time series shown in Fig. 3(b). The elastic precursor is evident and the plateau associated with the phase transformation is at a SiC-LiF particle velocity of ∼3.1 km/s, consistent with SiC stress of ∼100 GPa. The feature at ∼1.6 km/s is associated with a reverberation interaction between the elastic release from the LiF window and the oncoming plastic wave.

For the polycrystalline starting material, *in situ* XRD data were collected for two Hugoniot states, at ∼114 and ∼206 GPa, as determined from shots with LiF windows. For the single-crystal starting material, a Hugoniot state at ∼175 GPa was examined. For each compression state, a time series was collected by carrying out a sequence of shots on nominally identical samples (without LiF windows) using the same drive conditions as for the LiF-containing target and collecting XRD patterns at different probe times after the shock entered the sample. Data were recorded up to 40 ns after release from the free surface. The sample was probed with 8.5-keV free electron x rays focused to a 30-μm-diameter spot size near the center of the laser spot. The self-amplified spontaneous emission–mode x rays were quasimonochromatic (1% $\Delta E/E$) and consisted of 80-fs pulses containing $\sim 10^{12}$ photons. These short pulses enable snapshots of the compressed material, allowing for the exploration of kinetic effects.

The x-ray free electron laser beam makes an angle of 15° with the sample normal (Fig. 1). Diffraction is carried out in transmission geometry and scattered x rays are recorded on six Cornell-SLAC pixel array detectors (CSPADs) [41] positioned for wide angular coverage. We used three large-format (90-mm^2) and three small-format (43-mm^2) CSPAD detectors at distances ranging from 90 to 190 mm from the sample, allowing us to cover an approximately 15°–90° 2θ range (Supplementary Material, Fig. S8 [32]). The CSPAD data were projected to a common reference plane and integrated azimuthally to obtain one-dimensional XRD profiles. The CSPADs were calibrated using CeO_2, LaB_6, and Si_3N_4 standards.

Time series were collected by varying the time delay between the laser pulse and the probe x rays. The time at which the shock enters the SiC can be identified by a drop in reflectivity, as seen in the VISAR data (Supplemental Material, Fig. S6 [32]). This is designated $t = 0$ ns. Owing to the transmission geometry of the experiment, at times before the shock wave reaches the SiC free surface the x rays sample both the compressed material and the remaining uncompressed material ahead of the shock. A Hugoniot elastic limit of ∼26–29 GPa is determined from the measured wave profiles in Figs. 2 and S5 (Supplemental Material [32]). The elastic state is constrained to lie on the elastic Hugoniot of Vogler *et al.* [4]. We assume that the partial release at the SiC-LiF interface follows the elastic Hugoniot. By comparison, the reported Hugoniot elastic limit from gas-gun studies ranges from 11.5 to 18.9 GPa [5,9,10,42]. This enhancement of the elastic limit is consistent with reports of elevated elastic precursors in high-strain-rate laser-drive experiments in other materials [43,44].

The elastic precursor is not overdriven, and as a result, data recorded before shock breakout include evidence of elastically compressed material. At times after the shock wave has broken out at the SiC free surface, the x rays sample both compressed material and partially released material. The measured shock-wave transit times range from ∼3 to 5 ns, consistent with sample thicknesses of 40–60 μm and shock velocities determined by impedance matching. Experimental details for each shot are reported in the Supplemental Material, Tables S3 and S4 [32].

III. RESULTS

Figure 3 shows a time series of x-ray diffraction patterns for the polycrystalline starting material. The diffraction patterns shown are a sum of the six azimuthally integrated CSPAD images, where the intensity of each pattern has been rescaled in order to correct for background differences between detectors. XRD data were collected at variable probe times after the shock entered the SiC. The ambient 3C peaks are indexed in the preshot pattern.

Figure 3(a) shows a time series collected using drive conditions that produced a peak stress state of ∼206 GPa. At this stress, the shock transit time for the 40-μm SiC was ∼3 ns. Three patterns were recorded between 1.0 and 2.6 ns after the shock entered the sample and hence during

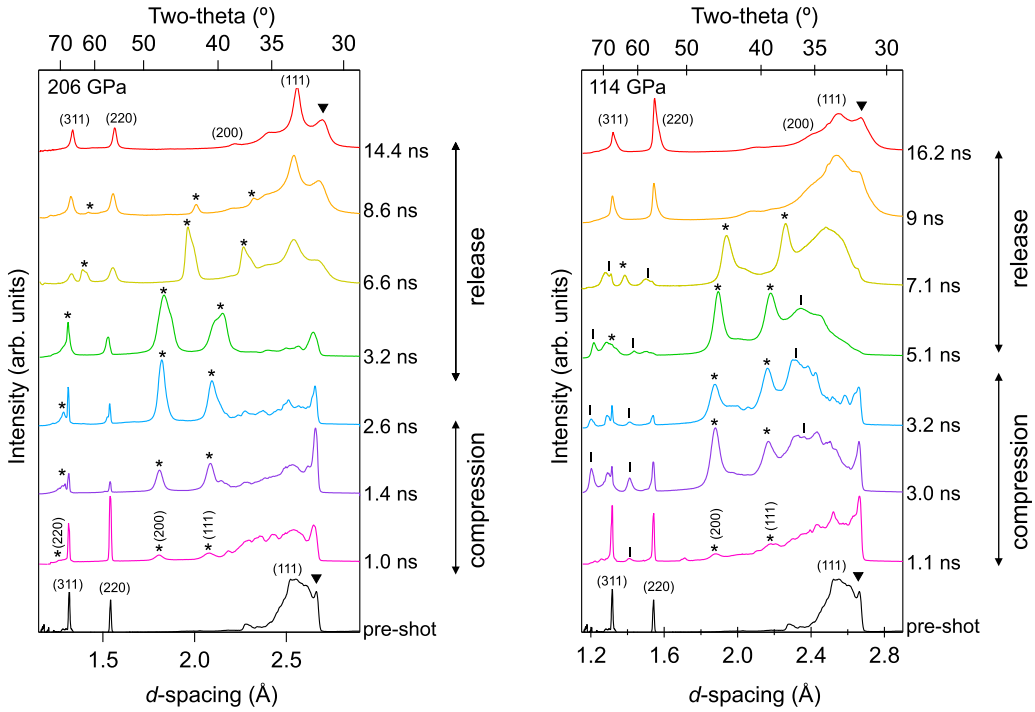

FIG. 3. (a) Integrated x-ray diffraction patterns for time series collected at a peak stress of ∼206 GPa for polycrystalline 3C starting material. X-ray probe times after the shock enters SiC are listed at the right. B1 peaks are marked with asterisks. Ambient 3C peaks are indexed in the preshot pattern. The feature marked with an inverted triangle at 2.66 Å arises due to stacking fault disorder (Supplemental Material, Fig. S1 [32]). Peaks from the back-transformed 3C phase are indexed in the top pattern. (b) Integrated diffraction patterns for time series collected for a peak stress of ∼114 GPa. B1 peaks and compressed 3C peaks are marked with asterisks and vertical lines, respectively. X-ray probe times after shock enters SiC are listed at the right.

the compression phase before the shock breakout. As a result, these patterns sample a uniform 206-GPa stress state along the Hugoniot. Peaks of the high-pressure B1 phase were observed at 1.0 ns after the shock entered the sample, the shortest delay time measured. This indicates that the 3C-B1 phase transition occurs rapidly under shock compression at this stress. We did not observe any evidence of peaks from the compressed 3C phase, indicating complete transformation to the B1 phase behind the shock front.

Figure 3(a) also shows four patterns recorded after breakout, at times ranging from 3.2 to 14.4 ns. As opposed to the patterns collected prior to breakout, the stress state upon release is heterogeneous, evidenced by both peak splitting and broadened peak profiles. The effects include both longitudinal release from the free surface and release waves from the lateral edges of the sample, giving rise to complex wave-wave interactions and resulting in a heterogeneous stress state in the region of the sample probed by the x-ray free electron laser.

Figure 3(b) shows a second time series of XRD patterns collected for the polycrystalline starting material at the lower peak stress of ∼114 GPa. The wave profile shown in Fig. 2 was collected using the drive conditions used for this series. The shock transit time for this series was ∼5 ns. Peaks from the transformed B1 phase as well as compressed 3C starting material are observed prior to breakout, indicating that the material is being shocked into a mixed-phase state. During this scan, four patterns were collected upon compression. After breakout, an additional three patterns were collected upon release. The B1 phase is retained for ∼2 ns after release and by 9 ns back transformation to the ambient 3C phase appears complete.

Figure 4 shows the results from a time series collected with a peak stress of ∼175 GPa for the single-crystal α-SiC starting material. Similar to the polycrystalline samples, the single crystal rapidly transforms to a B1 structure upon loading. The samples were oriented such that there were no single-crystal diffraction spots from the ambient α-SiC starting material recorded on the CSPAD detectors. As a result, no ambient diffraction is recorded during the compression phase for these shots. Here the transit time was ∼3 ns and the majority of the diffraction data were collected after breakout. Similar to the polycrystalline starting material, a large hysteresis is observed upon back transformation, where the B1 phase is retained for nearly 10 ns after release. Upon release the pattern can be indexed as a combination of ambient 3C and 4H phases. A profile refinement was carried out for the pattern collected at the latest probe time (43.1 ns) using the GSAS package [45,46]. The refinement indicates that the sample released to ambient conditions consists of 48% 3C and 52% 4H polymorphs (Supplemental Material, Fig. S7 [32]).

IV. DISCUSSION

Figure 5 summarizes the evolution of d spacings as a function of the probe time, determined from fits to diffraction patterns for the time series shown in Fig. 3(a). Figure 5 also reports results from additional shots not shown in Fig. 3(a). Results for all shots are included in the Supplemental

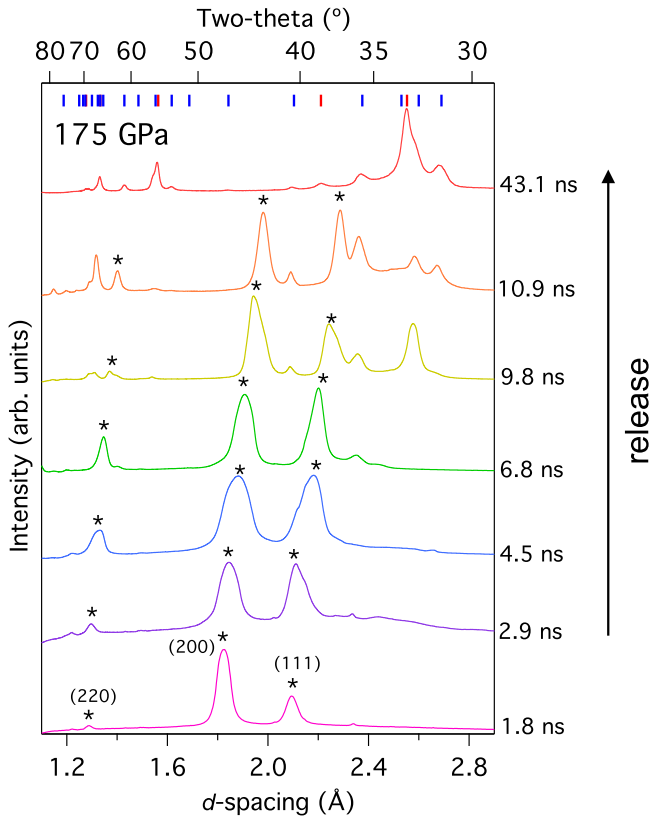

FIG. 4. Integrated diffraction patterns for time series collected at a peak stress of ∼175 GPa for single-crystal α-SiC starting material (4H). X-ray probe times after the shock enters SiC are listed at the right. B1 peaks are marked with asterisks. For the latest probe time (43.1 ns), the pattern can be indexed with a combination of 3C (red) and 4H (blue) peaks, indicated by tick marks above the pattern.

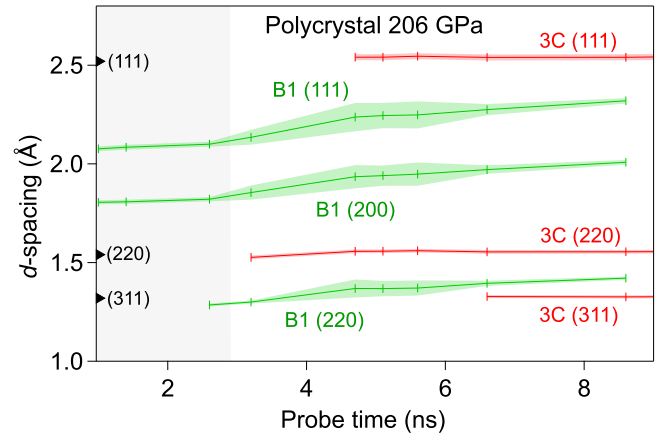

FIG. 5. The d spacings for polycrystalline SiC determined from fits to x-ray diffraction patterns for the time scan shown in Fig. 3(a) as a function of the time after the shock has entered the SiC. The trends are the result of a linear extrapolation between the discrete probe times (hash marks). Shaded regions indicate the uncertainties in d spacings and encompass the range of d spacings that arise from sampling a nonhomogenous stress state after breakout. The gray area contains results from shots collected on compression, prior to breakout. Ambient 3C peak positions are shown by black triangles at the left.

Material, Table S3 [32]. In Fig. 5, The B1 (111) and (200) peaks appear at the earliest measured probe time (1 ns). The position of the B1 (220) peak cannot be determined prior to breakout as a result of its relatively low intensity and overlap with the uncompressed (311) 3C peak. The d spacings for the transformed B1 phase remain unchanged up to the shock breakout time at 3 ns, after which the peaks shift to a higher d spacing as the pressure in the sample decreases. At these later times, the diffraction peaks exhibit both peak splitting and pronounced profile broadening [Fig. 3(a)]. This reflects a stress distribution in the sample as a dispersive release wave propagates back from the free surface. In Fig. 5, the fan of d spacings between 3 and 7 ns captures the range of peak positions spanned by the broadened B1 lines.

In addition to probing phases on the Hugoniot, the time resolution of our measurements allows us to directly observe a large hysteresis in the back transformation to the ambient four-coordinated structure(s). The B1 phase is retained for more than 5 ns after release before reversion to the ambient 3C phase. In Fig 5, at ∼7–8 ns, the B1 peaks resharpen, indicating that the material has returned to a homogeneous stress state. This suggests that the B1 phase is retained to near-ambient pressure. At 8.6 ns, only a small trace of the high-pressure phase remains, and by 14.4 ns back transformation is complete [Fig. 3(a)].

Figure 6 shows the densities determined by XRD under shock loading along with reported densities from previous gas-gun [4,5] and diamond-anvil-cell studies at 300 K [16–19]. For the three time series discussed above (Figs. 3 and 4), the XRD densities (Fig. 6) were determined from data recorded prior to breakout and thus represent material compressed to a uniform stress state on the Hugoniot. Owing to the uniaxial compression geometry in our experiments, we measured longitudinal stress. Figure 6 also shows a 300 K EOS for the 3C and B1 phases, determined from diamond-anvil-cell data [19,47].

Figure 6 includes a theoretical B1 Hugoniot calculated using a Mie-Grüneisen EOS (Supplemental Material, Fig. S3 [32]). A comparison of the calculated Hugoniot to the densities determined from XRD demonstrates that our results are consistent with the expected properties of the B1 phase along the Hugoniot. The thermodynamic parameters used to calculate the B1 Hugoniot in Fig. 6 are listed in the Supplemental Material, Table S2 [32]. The calculation incorporates a 3C-B1 transition energy from density functional theory calculations [20] along with the set of thermodynamic parameters determined from a fit to diamond-anvil-cell results [19]. As the Grüneisen parameter (γ_0) is not well constrained experimentally, the Hugoniot was calculated for the range $\gamma_0 = 0.5$ to $\gamma_0 = 2$, giving rise to the gray field in Fig. 6. The stresses shown for the two time series collected above 150 GPa in Fig. 6 were determined assuming an extrapolation of the gas-gun Hugoniot data of Vogler *et al.* [4]. Further experimental studies are needed to better constrain the Hugoniot above 1 Mbar.

For the time series at 206 and 175 GPa, the B1 densities from XRD are consistent with the calculated Hugoniot. For the polycrystalline time series at 114 GPa, we observed the coexistence of the compressed 3C phase and transformed B1

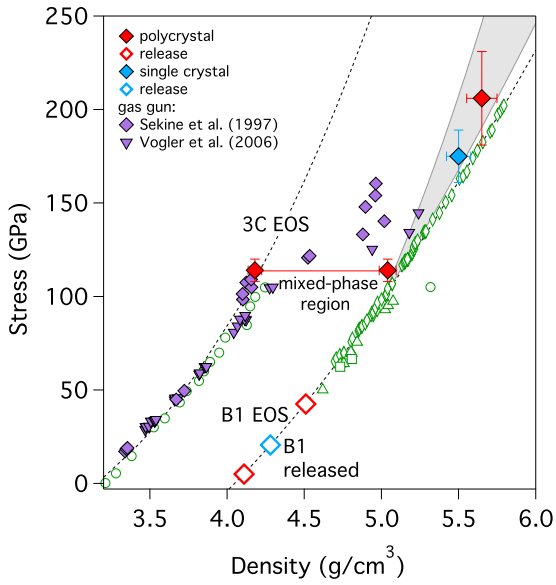

FIG. 6. The present results (red and blue symbols) compared to continuum gas-gun results (purple symbols) [4,5]. Static 300 K studies are shown as open green symbols; results of Yoshida *et al.* [16], Daviau *et al.* [17], Miozzi *et al.* [19], and Kidokuro *et al.* [18] are represented by circles, squares, diamonds, and triangles, respectively. The present Hugoniot data are more consistent with the gas-gun results of Vogler *et al.* [4] than of Sekine *et al.* [5] and lie close to the calculated theoretical Hugoniot (gray shaded region). The densities of the two components of the mixed-phase region lie close to the 3C Hugoniot curve and the calculated B1 Hugoniot. The 300 K B1 equation of state (EOS) and the 3C EOS calculated from static compression data [19] are shown as dashed black curves.

phase. The densities of these phases fall on the measured 3C Hugoniot and the theoretical B1 Hugoniot, respectively. The densities for the coexisting phases observed during compression suggest a volume collapse of 16%, consistent with previous diamond-anvil-cell studies [13,16,17]. In Fig. 6, the coexisting compressed 3C and transformed B1 phase are both plotted at the peak stress of 114 GPa despite ambiguity as to whether the XRD samples a metastable mixed-phase assemblage or a multiwave structure.

Figure 6 shows B1 densities from data collected upon release (open symbols), corresponding to the last shot in a given time series for which the B1 phase was observed (i.e., the lowest-density B1 phase observed). The release densities have been placed on the B1 300 K EOS [19]. While the release pressure-temperature state is not well constrained experimentally, the relatively low thermal expansion of SiC [26] makes the 300 K isotherm a reasonable first-order approximation. A comparison of these release densities to the theoretical ambient volume of the B1 phase suggests that the B1 phase is retained to pressures as low as 5 GPa. This requires a substantial volume expansion of the B1 unit cell to occur within nanoseconds. For the highest-stress shot, we observed a 38% volume expansion of the B1 phase relative to its Hugoniot density upon unloading prior to reversion to the ambient structure.

Under shock loading and release we observe a direct transformation to the B1 crystal structure followed by a reversion to the ambient phase on the nanosecond time scales of our measurements, with no evidence of the formation of any intermediate phases. Our results suggest that the pathway through any transient structures must proceed on a subnanosecond time scale. This interpretation is consistent with *ab initio* molecular dynamics simulations indicating that the transition to the B1 phase occurs as quickly as 0.1 ps [48]. Accordingly, experiments targeted at probing intermediate structures experimentally require femtosecond x-ray diffraction techniques.

Our XRD measurements provide crystallographic evidence of the phase transition from the four-coordinated 3C and 4H structures to the B1 phase under shock compression. Our results are consistent with the transition inferred from continuum gas-gun data, despite largely different time scales (nanosecond versus hundreds of nanoseconds). The densities determined from XRD are in reasonable agreement with continuum measurements and/or the theoretical Hugoniot derived from static measurements. Our study represents a significant extension of previous gas-gun and diamond-anvil-cell results, reaching stress states in excess of 2 Mbar while providing new details of the hysteresis in the B1 transformation upon unloading.

ACKNOWLEDGMENTS

We thank Eran Greenberg (University of Chicago), Dongzhou Zhang (University of Hawaii), and the target fabrication team at Lawrence Livermore National Laboratory for experimental assistance. Gregory Stewart (SLAC) provided the graphic of the experimental configuration. Support for this research was provided by U.S. Department of Energy (DOE), Office of Science, Fusion Energy Sciences Grant No. DE-SC00016242 and performed under the auspices of the DOE by Lawrence Livermore National Laboratory under Contract No. DE-AC52-07NA27344. Use of the Linac Coherent Light Source (LCLS), SLAC National Accelerator Laboratory, was supported by the DOE, Office of Science, Office of Basic Energy Sciences, under Contract No. DE-AC02-76SF00515.

[1] H. O. Pierson, in *Handbook of Refractory Carbides and Nitrides* (William Andrew, Westwood, NJ, 1996), p. 362.

[2] K. A. Schwetz, in *Handbook of Ceramic Hard Materials*, edited by R. Riedel (Wiley-Blackwell, Hoboken, NJ, 2008), pp. 683–748.

[3] T. J. Holmquist and G. R. Johnson, J. Appl. Phys. **91**, 5858 (2002).

[4] T. J. Vogler, W. D. Reinhart, L. C. Chhabildas, and D. P. Dandekar, J. Appl. Phys. **99**, 023512 (2006).

[5] T. Sekine and T. Kobayashi, Phys. Rev. B **55**, 8034 (1997).

[6] R. M. Hough, I. Glimour, C. T. Pillinger, J. W. Arden, K. W. R. Gilkes, J. Yuan, and H. J. Milledge, Nature **378**, 41 (1995).

[7] R. B. Trumbull, J.-S. Yang, P. T. Robinson, S. D. Pierro, T. Vennemann, and M. Wiedenbeck, Lithos **113**, 612 (2009).

[8] W. H. Gust, A. C. Holt, and E. B. Royce, J. Appl. Phys. **44**, 550 (1973).

[9] D. E. Grady, J. Phys. IV France **04**, 385 (1994).

[10] R. Feng, G. F. Raiser, and Y. M. Gupta, J. Appl. Phys. **83**, 79 (1998).

[11] P. S. Branicio, J. Zhang, J. P. Rino, A. Nakano, R. K. Kalia, and P. Vashishta, Appl. Phys. Lett. **112**, 111909 (2018).

[12] K. Daviau and K. K. M. Lee, Crystals **8**, 217 (2018).

[13] W. A. Bassett, M. S. Weathers, T. Wu, and T. Holmquist, AIP Conf. Proc. **309**, 145 (1994).

[14] M. Catti, Phys. Rev. Lett. **87**, 035504 (2001).

[15] P. Bogusławski and J. Bernholc, in *Encyclopedia of Materials: Science and Technology*, edited by K. J. Buschow, R. W. Cahn, M. C. Flemings, B. Ilschner, E. J. Kramer, S. Mahajan, and P. Veyssière (Elsevier, Oxford, UK, 2001), pp. 7131–7139.

[16] M. Yoshida, A. Onodera, M. Ueno, K. Takemura, and O. Shimomura, Phys. Rev. B **48**, 10587 (1993).

[17] K. Daviau and K. K. M. Lee, Phys. Rev. B **95**, 134108 (2017).

[18] Y. Kidokoro, K. Umemoto, K. Hirose, and Y. Ohishi, Am. Mineral. **102**, 2230 (2017).

[19] F. Miozzi, G. Morard, D. Antonangeli, A. N. Clark, M. Mezouar, C. Dorn, A. Rozel, and G. Fiquet, J. Geophys. Res.: Planets **123**, 2295 (2018).

[20] K. Karch, F. Bechstedt, P. Pavone, and D. Strauch, Phys. Rev. B **53**, 13400 (1996).

[21] Y.-P. Lu, D.-W. He, J. Zhu, and X.-D. Yang, Phys. B **403**, 3543 (2008).

[22] W. H. Lee and X. H. Yao, Comput. Mater. Sci. **106**, 76 (2015).

[23] F. Shimojo, I. Ebbsjö, R. K. Kalia, A. Nakano, J. P. Rino, and P. Vashishta, Phys. Rev. Lett. **84**, 3338 (2000).

[24] M. Catti, Phys. Rev. B **65**, 224115 (2002).

[25] H. F. Wilson and B. Militzer, Astrophys. J. **793**, 34 (2014).

[26] C. Nisr, Y. Meng, A. A. MacDowell, J. Yan, V. Prakapenka, and S.-H. Shim, J. Geophys. Res.: Planets **122**, 124 (2017).

[27] T. S. Duffy, N. Madhusudhan, and K. K. M. Lee, in *Treatise on Geophysics*, 2nd ed., edited by G. Schubert (Elsevier, Oxford, UK, 2015), pp. 149–178.

[28] K. Daviau and K. K. M. Lee, Phys. Rev. B **96**, 174102 (2017).

[29] M. G. Gorman, A. L. Coleman, R. Briggs, R. S. McWilliams, D. McGonegle, C. A. Bolme, A. E. Gleason, E. Galtier, H. J. Lee, E. Granados, M. Śliwa, C. Sanloup, S. Rothman, D. E. Fratanduono, R. F. Smith, G. W. Collins, J. H. Eggert, J. S. Wark, and M. I. McMahon, Sci. Rep. **8**, 16927 (2018).

[30] P. Kalita, P. Specht, S. Root, N. Sinclair, A. Schuman, M. White, A. L. Cornelius, J. Smith, and S. Sinogeikin, Phys. Rev. Lett. **119**, 255701 (2017).

[31] Y. Syono, K. Kusaba, T. Atou, and K. Fukuoka, in *Shock Waves*, edited by K. Takayama (Springer, Berlin, 1992), pp. 121–128.

[32] See Supplemental Material at http://link.aps.org/supplemental/10.1103/PhysRevB.99.214106, which includes Refs. [32–37], for details concerning the experimental procedure, data reduction, and analysis.

[33] S. Nakashima and H. Harima, Phys. Status Solidi (a) **162**, 39 (1997).

[34] S. Nakashima, H. Makoto, M. Kouji, and T. Hidehiko, J. Am. Ceram. Soc. **86**, 823 (2004).

[35] P. M. Celliers, D. K. Bradley, G. W. Collins, D. G. Hicks, T. R. Boehly, and W. J. Armstrong, Rev. Sci. Instrum. **75**, 4916 (2004).

[36] R. G. McQueen, S. P. Marsh, J. W. Taylor, J. N. Fritz, and W. J. Carter, in *High Velocity Impact Phenomena*, edited by R. Kinslow (Academic Press, New York, 1970), pp. 294–417.

[37] Q. Liu, X. Zhou, X. Zeng, and S. N. Luo, J. Appl. Phys. **117**, 045901 (2015).

[38] B. Nagler, B. Arnold, G. Bouchard, R. F. Boyce, R. M. Boyce, A. Callen, M. Campell, R. Curiel, E. Galtier, J. Garofoli, E. Granados, J. Hastings, G. Hays, P. Heimann, R. W. Lee, D. Milathianaki, L. Plummer, A. Schropp, A. Wallace, M. Welch, W. White, Z. Xing, J. Yin, J. Young, U. Zastrau, and H. J. Lee, J. Synchrotron Radiat. **22**, 520 (2015).

[39] S. B. Brown, A. Hashim, A. Gleason, E. Galtier, I. Nam, Z. Xing, A. Fry, A. MacKinnon, B. Nagler, E. Granados, and H. J. Lee, Rev. Sci. Instrum. **88**, 105113 (2017).

[40] T. J. Ahrens, in *Geophysics, Methods in Experimental Physics*, edited by G. H. Sammis and T. L. Henyey (Academic Press, New York, 1987), Vol. 24, pp. 185–235.

[41] H. T. Philipp, M. Hromalik, M. Tate, L. Koerner, and S. M. Gruner, Nucl. Instrum. Methods Phys. Res. Sec. A: Accelerat. Spectrom. Detect. Assoc. Equip. **649**, 67 (2011).

[42] N. Bourne, J. Millett, and I. Pickup, J. Appl. Phys. **81**, 6019 (1997).

[43] R. F. Smith, R. W. Minich, R. E. Rudd, J. H. Eggert, C. A. Bolme, S. L. Brygoo, A. M. Jones, and G. W. Collins, Phys. Rev. B **86**, 245204 (2012).

[44] R. F. Smith, J. H. Eggert, R. E. Rudd, D. C. Swift, C. A. Bolme, and G. W. Collins, J. Appl. Phys. **110**, 123515 (2011).

[45] C. Larson and R. V. Dreele, *General Structure Analysis System (GSAS)*, Technical Report LAUR 86-748 (Los Alamos National Laboratory, Los Alamos, NM, 1994).

[46] B. H. Toby, J. Appl. Crystallogr. **34**, 210 (2001).

[47] K. K. Zhuravlev, A. F. Goncharov, S. N. Tkachev, P. Dera, and V. B. Prakapenka, J. Appl. Phys. **113**, 113503 (2013).

[48] H. Y. Xiao, F. Gao, L. M. Wang, X. T. Zu, Y. Zhang, and W. J. Weber, Appl. Phys. Lett. **92**, 241909 (2008).